

Weierstraß-Institut
für Angewandte Analysis und Stochastik
Leibniz-Institut im Forschungsverbund Berlin e. V.

Preprint

ISSN 0946 – 8633

**Measurement and simulation of a droplet population in a
turbulent flow field**

Róbert Bordás¹ , Volker John², Ellen Schmeyer² , Dominique Thévenin¹

submitted: May 16, 2011

¹ University of Magdeburg
"Otto von Guericke"
Universitätsplatz 2
39106 Magdeburg
Germany
email: bordas@ovgu.de
email: thevenin@ovgu.de

² Weierstrass Institute
for Applied Analysis and Stochastics
Mohrenstr. 39
10117 Berlin
Germany
email: Volker.John@wias-berlin.de
email: Ellen.Schmeyer@wias-berlin.de

No. 1590
Berlin 2011



2010 *Mathematics Subject Classification.* 76F65,76T10.

Key words and phrases. two-phase turbulent flow, disperse droplet population, non-intrusive measurements, population balance systems, variational multiscale method.

Edited by
Weierstraß-Institut für Angewandte Analysis und Stochastik (WIAS)
Leibniz-Institut im Forschungsverbund Berlin e. V.
Mohrenstraße 39
10117 Berlin
Germany

Fax: +49 30 2044975
E-Mail: preprint@wias-berlin.de
World Wide Web: <http://www.wias-berlin.de/>

Abstract

The interaction of a disperse droplet population (spray) in a turbulent flow field is studied by combining wind tunnel experiments with simulations based on the model of a population balance system. The behavior of the droplets is modeled numerically by a population balance equation. Velocities of the air and of the droplets are determined by non-intrusive measurements. A direct discretization of the 4D equation for the droplet size distribution is used in the simulations. Important components of the numerical algorithm are a variational multiscale method for turbulence modeling, an upwind scheme for the 4D equation and a pre-processing approach to evaluate the aggregation integrals. The simulations of this system accurately predict the modifications of the droplet size distribution from the inlet to the outlet of the measurement section. Since the employed configuration is simple and considering that all measurement data are freely available thanks to an Internet-based repository, the considered experiment is proposed as a benchmark problem for the simulation of disperse two-phase turbulent flows.

1 Introduction

In this paper detailed numerical simulations of systematic experimental studies concerning droplet populations interacting with a turbulent flow are presented. Such investigations are important to characterize modifications in the Droplet Size Distribution (DSD) resulting from droplet/droplet interactions induced by turbulent structures. Water droplets with an initial diameter up to 50 μm are injected into a Göttingen-type wind tunnel with a closed test section. Velocities of both phases (air and

droplets) are carefully determined by means of non-intrusive measurement techniques. In this way, suitable boundary conditions and data are available to validate corresponding numerical simulations.

All measurement data are collected in an online database accessible at www.ovgu.de/isut/lss/metstroem. The raw measurement results are further post-processed, so that all required data are in a suitable form for comparisons and validation.

The behavior of the droplet population is modeled by means of a population balance system, consisting of the Navier–Stokes equations describing the air flow together with an additional equation for the DSD. In this last equation, the transport, growth, and aggregation of droplets is taken into account. The DSD describes the spatial evolution of the diameter of the droplets, the so-called internal coordinate, such that the equation for the DSD is finally defined in a 4D domain.

Population balance systems can be applied for modeling many processes in engineering and nature, like precipitation and crystallization processes, or rain formation. The development of accurate and efficient numerical methods for such simulations is an active field of research. Several suitable approaches have been proposed in the literature. In particular, moment-based methods like the quadrature method of moments (QMOM) [31], in which the equation in the 4D domain is replaced by a system of equations for the moments defined in the 3D flow domain, appears promising. A possible extension of QMOM is the direct quadrature method of moments (DQMOM) [30]. Further, operator splitting techniques have been studied recently [8], projecting the solution of the 4D problem onto the solution of a 1D problem followed by the solution of a 3D problem. Moment-based approaches and operator splitting schemes are beneficial, since the solution of the 4D equation is not needed any more. On the other hand, additional errors are introduced.

In the present paper, a direct discretization of the 4D equation for the DSD is retained, since the accuracy of the results is here more important than the numerical efficiency of the simulations. Simulations based on the 4D equation can be found rather rarely in the literature. However, with increasing hardware capabilities and with modern numerical methods, this is an attractive approach since it does not require any additional assumptions, e.g., for closing the system, and it does not introduce an additional modeling error. In the used method, the turbulent flow field is simulated fully implicitly. A variational multiscale (VMS) method is applied for turbulence modeling. The backward and forward Euler scheme are used as temporal discretization for the population balance equation. A pre-processing approach was applied to compute the aggregation integrals. With this numerical approach, it will be shown that the experimentally observed evolution of the DSD between the inlet of the flow domain and its outlet can be reproduced accurately. The robustness of the prediction with respect to varying numerical methods is demonstrated. To our best knowledge, the combination of the used methods for simulating a population balance system cannot be found so far in the literature.

The retained configuration corresponds to an experiment proposed as a benchmark problem for the simulation of population balance systems, since

- all data are freely available in the online database at www.ovgu.de/isut/lss/metstroem,
- the considered geometry and setup is simple,
- first numerical studies are already available, supporting the accuracy of the experimental measurements.

The paper is organized as follows. The experimental setup is first described in Section 2, followed by the measurements and the post-processing procedure in

Section 3. Section 4 describes the population balance system used to model the experiments. The numerical methods employed to simulate this setup are discussed in Section 5 and the simulation results are presented in Section 6. A summary is proposed at the end of the paper.

2 Experimental Setup

A special wind tunnel available at the laboratory of Fluid Dynamics & Technical Flows has been used for the present experimental investigation of disperse two-phase flows corresponding to meteorological conditions found in cumulus clouds [4, 5]. This wind tunnel can be used to investigate a variety of two-phase (air/liquid) flows [12], see Fig. 1. It is a fully computer-controlled, Göttingen-type wind tunnel. Operation with a closed test section enables the controlled and reproducible investigation of two-phase mixtures in the test section. The test section is of size $H \times W \times L = 500 \times 600 \times 1500$ mm. It includes a measurement section of cross-section 450×500 mm whose windows are optically transparent in the visible spectrum. In this manner non-intrusive measurements are possible, which is essential for high-quality experimental investigations of such flows.

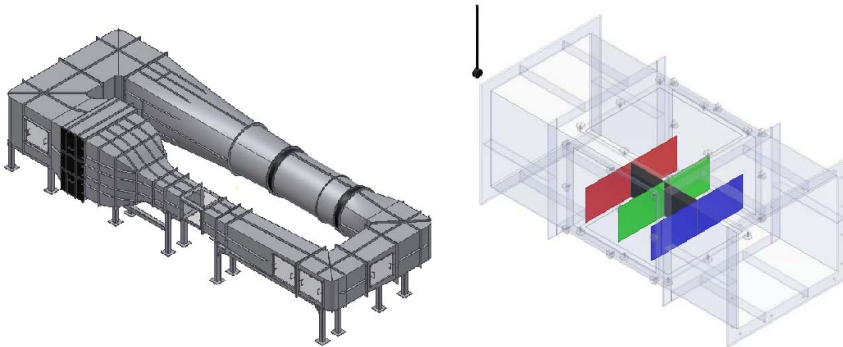


Figure 1: Left: Göttingen-type two-phase wind tunnel with closed test section. Right: test section, with measurement planes colored.

The disperse phase was added to the air flow with the help of an injection system. The sprays were actuated by means of eccentric screw pumps. The number of revolutions per minute (rpm) was set with the help of a frequency regulator to a prescribed value by means of a Proportional Integral Derivative (PID) regulation coded in LabView[®]. In order to investigate rain formation and cloud droplet interactions a full cone pneumatic atomizing nozzle was used (Type 166.208.16.12 from the company Lechler GmbH), relying on the liquid pressure principle and applying an air gauge pressure of 1.2 bar [3].

Since the influence of the support of the injection system could be noticed especially in the upper half of the measurement section, the measurement area was finally restricted to the lower half of the cross-section, see Fig. 2. The resulting velocity inhomogeneity of the air flow was then below 5% with a turbulence intensity below 7% (mean value of 2.4%). The selected nozzle shows a typical six-hole spray pattern caused by the six orifices in the nozzle. In order to reduce the influence of this pattern, the water was injected in counter-flow direction. In this way, the droplets were more homogeneously distributed, and the relative velocity difference between continuous and dispersed flow at the entrance of the measurement section was decreased, suppressing to a large extent the six-hole pattern.

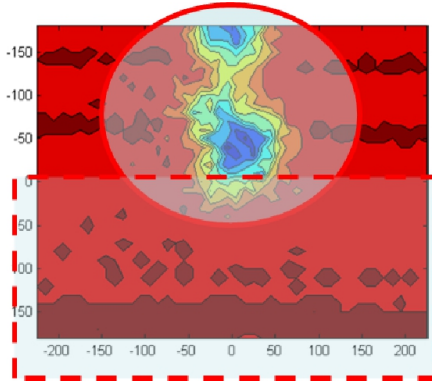


Figure 2: Mean axial velocity distribution of the air flow at the inlet ($x = 0$ mm) of the measurement section, 630 mm downstream of the spray injection nozzle. The circle denotes the region with a noticeable influence of the injection mount and the dashed square the finally selected measurement region.

3 Measurement Procedure

The longitudinal coordinate of the beginning of the measurement section is defined as $x = 0$ mm. Different measurement planes perpendicular to the main flow direction were investigated, at $x = 0$ mm, $x = 200$ mm, and $x = 400$ mm, see Fig. 1. The first plane at $x = 0$ mm was measured particularly thoroughly, since it provides the information needed for the boundary condition of the numerical simulations.

Experimental measurements were systematically carried out by means of non-intrusive measurement techniques. Therefore, a small quantity of suitable tracer particles must be added to the flow. Such particles follow the structures of the continuous phase much better [1, 2] than the considered droplets, allowing an indirect measure of the gas flow properties. For this reason, the velocities of both phases were measured in two separate steps.

The velocity distribution of the air phase at the entrance plane ($x = 0$ mm) was measured by means of Laser-Doppler Velocimetry (LDV). During these measurements in the continuous phase, the nozzle was operating at the same pressure as in normal (spray) operation, but only with air and without water. Since the mass flow rate of air and water in normal operation conditions are similar, $\dot{m}_a/\dot{m}_w = 0.4$, only minor flow changes should be induced by this necessary operation.

In order to define the locations of the measurement points for the Laser-Doppler Velocimetry and the Phase-Doppler Anemometry (PDA) techniques, a measurement grid was generated with 874 (19 in z -direction \times 46 in y -direction) measurement points, with 10 mm distance in each direction between them. LDV and PDA measurements lead to a high temporal resolution. Thus, the velocity components measured in the mean flow direction (Fig. 3) included the temporal fluctuations as well. In this way, the determination of turbulence intensity was also possible.

The measured mean velocity of the air flow was $U = 2.45$ m/s. Based on U and on the hydraulic diameter of the wind tunnel ($D_H = 0.5454$ m), the Reynolds number of the flow is

$$\text{Re} = \frac{U \cdot D_H}{\nu} = 8.7 \cdot 10^4.$$

The measured fluctuation of the air flow velocity in main flow direction was in the average $u' = 0.25$ m/s. This leads to a mean turbulence intensity of 10.92%.

The properties of the disperse phase (water spray) were then measured separately in the three vertical planes at $x = 0$ mm, $x = 200$ mm, and $x = 400$ mm,

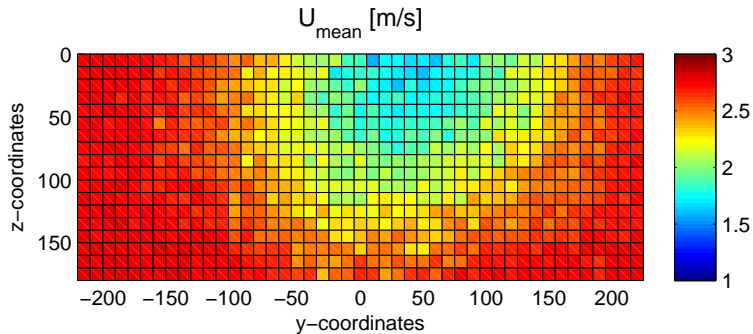


Figure 3: Mean longitudinal velocity distribution of the air phase at $x = 0$ mm, measured by means of LDV.

of course using the same measurement grid as previously. For a characterization of the considered two-phase flow, the arithmetic mean diameter (D_{10}) of the water droplets is particularly important.

Velocities measured by PDA are based on the same principles as LDV. However, using PDA the simultaneous measurement of the diameter and the velocity values is possible. This allowed the investigation of the velocity-diameter correlation, as exemplified in Fig 4. The different flow response of the droplets can be noticed in this scatter plot. Due to noticeable smaller Stokes numbers, the small droplets follow much more closely the fluctuations of the turbulent flow and are therefore associated with larger velocity fluctuations, while larger droplets tend to gather around the mean velocity value. Having the velocity values of both phases, the relative velocity difference of the droplets can finally be calculated. This was found to be 0.3 m/s in average at $x = 0$ mm. This value reduced as expected to 0.15 m/s as the droplets reached the final measurement plane $x = 400$ mm, showing that the droplets are slightly accelerating on the way from the inlet to the outlet plane. The mean velocity of the droplets, measured by means of PDA for the planes $x = 0$ mm, $x = 200$ mm and $x = 400$ mm, is shown in Fig 5. These data were used, in combination with the turbulent air flow, to interpolate the velocity of the droplets \mathbf{u}_{drop} from the measurement planes to the whole domain, see Sect. 4.

Boundary conditions for the droplet size distribution at $x = 0$ mm have to be derived from the measurements in order to start the companion simulations. At the outlet boundary ($x = 400$ mm), experimental data are needed as well for comparison purposes. Therefore, a corresponding post-processing of the PDA measurements is necessary to obtain values for the number density or droplet concentration n [36, 39]. In the present work, the approach described in [13] was finally applied, improved by a correction factor η_{vi} allowing to correct errors due to multiple particles occurring in the detection volume or to non-validation of particles, as described by [37]. The droplet size dependent calculation of the detection volume [37] was applied as well. Thus, the number density is finally obtained by

$$n = \frac{1}{T_{\text{acq}}} \sum_{i=1}^{N_{\text{sv}}} \frac{\eta_{vi} \cdot t_{\text{res},i}}{V_{\text{det}}}, \quad (1)$$

where T_{acq} is the acquisition time at a given measurement position, N_{sv} is the number of validated PDA-signals, η_{vi} is the correction factor described before, $t_{\text{res},i}$ is the residence time of the i^{th} droplet and V_{det} is the size of the PDA detection volume. The PDA detection volume is droplet size dependent and thus is a function of the droplet velocity and of the burst duration in the detection volume.

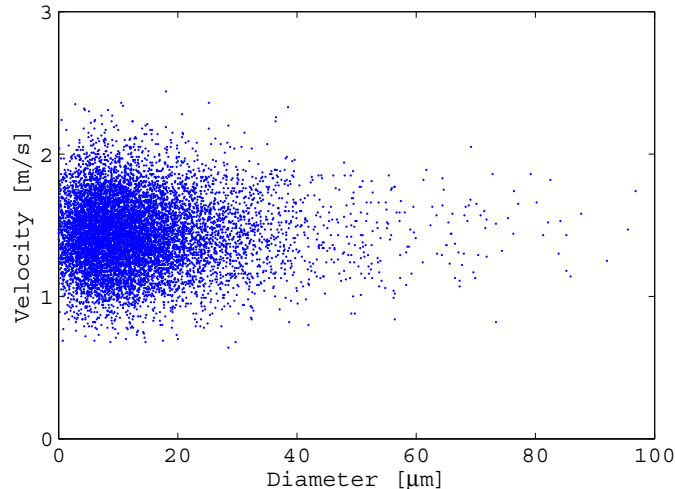


Figure 4: Velocity-diameter correlation of the water droplets at the point $x = 0$, $y = 5$, $z = 0$.

The average mean droplet number density per unit volume was finally measured to be 2000 no./cm^3 at $x = 0 \text{ mm}$. The corresponding distribution of the mean values is presented in Fig. 6. Theoretically, with a droplet injection rate of 0.1 l/min and a mean droplet diameter of $12.5 \mu\text{m}$, the corresponding droplet number density per unit volume should be indeed approximately 2000 no./cm^3 , supporting the experimental measurements. This droplet number density per unit volume is in the range of typical values found in cumulus clouds [28].

The determination of the probability density function $n_k(d_k)$ is the key link between experimental data and numerical simulations. The corresponding post-processing was performed with a MATLAB[®] script, using the previously exported measurement raw data, and allowing both the computation of the probability density function of the droplet number density ($n_k(d_k)$) and its standard deviation ($\sigma_{n,k}$). The droplets are divided into classes (d_k) with a diameter resolution of $2 \mu\text{m}$. The number density is computed separately for each size class using Eq.(1). In addition, the number density was calculated for different time scales by dividing the whole acquisition time T_{acq} into time intervals Δt . In this manner, the standard deviation $\sigma_{n,k}$ can be calculated with

$$\sigma_{n,k} = \sqrt{\left(\frac{1}{T_{\text{acq}}} \sum_{j=1}^{T_{\text{acq}}/\Delta t} n_{k,j}^2 \cdot \Delta t \right) - n_k^2}.$$

The input data for the simulations are then the droplet concentration as a function of the droplet diameter, together with the corresponding standard deviation, as shown in Fig. 7 for the entrance plane ($x = 0 \text{ mm}$).

4 Numerical Model of the Process

The experiment is modeled using a coupled equation system consisting of the Navier–Stokes equations for describing the air flow and a population balance equation modeling the behavior of the droplet size distribution. Only the lower half of the test section is simulated, in agreement with the experimental approach described previously, see again Fig. 2.

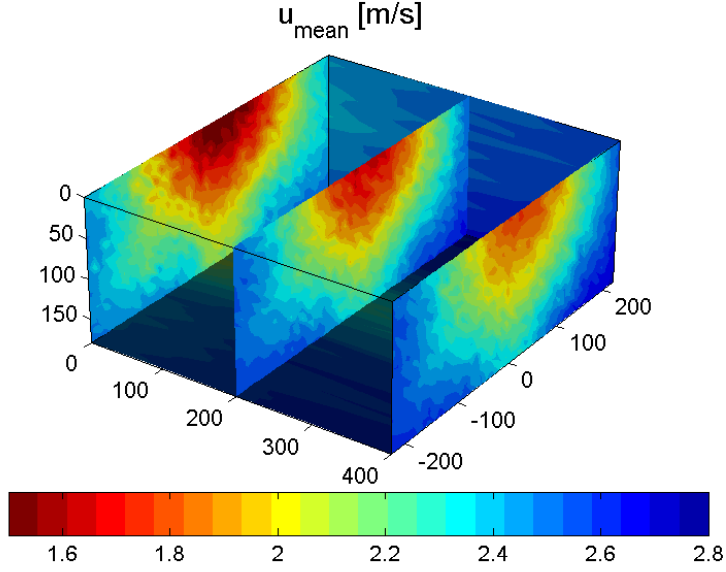


Figure 5: Mean droplet velocity distribution in the planes $x = 0$ mm, $x = 200$ mm, and $x = 400$ mm measured by means of PDA.

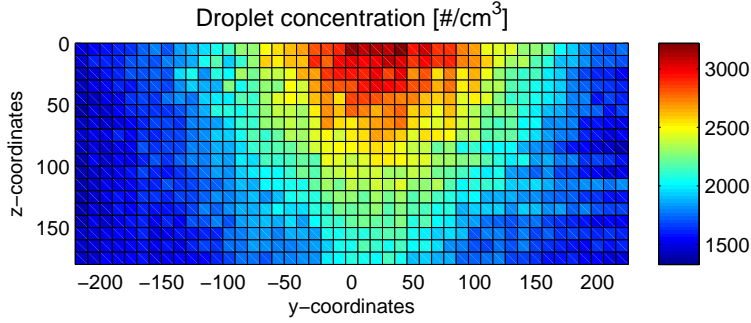


Figure 6: Droplet number density per unit volume in no./cm³ at $x = 0$ mm, post-processed from the PDA results.

Boundary conditions for the flow field have to be prescribed at the whole boundary of the domain used in the simulations. It is not clear if the used outflow boundary condition, associated with zero normal stresses, introduces a noticeable modeling error. For this reason, the domain for the simulations was chosen to be somewhat longer than the real measurement domain, so that the outflow boundary condition did not influence the computational results at the locations where comparisons are possible. The final computational domain was set to be $\Omega = (0, 500) \times (-225, 225) \times (-180, 0)$ mm³ for x, y and z , respectively, with z corresponding to standard elevation.

The incompressible Navier–Stokes equations have the form

$$\begin{aligned} \rho \mathbf{u}_t - 2\mu \nabla \cdot \mathbb{D}(\mathbf{u}) + \rho(\mathbf{u} \cdot \nabla) \mathbf{u} + \nabla p &= \mathbf{0} & \text{in } (0, t_e) \times \Omega, \\ \nabla \cdot \mathbf{u} &= 0 & \text{in } (0, t_e) \times \Omega, \end{aligned} \quad (2)$$

where \mathbf{u} (m/s) is the fluid velocity vector, p (Pa) is the pressure, $\rho = 1.2041$ kg/m³, assumed to be constant due to the extremely low Mach number considered here, is the density of air at 293.15 K, $\mu = 18.15 \cdot 10^{-6}$ kg/(m s) is the dynamic viscosity of

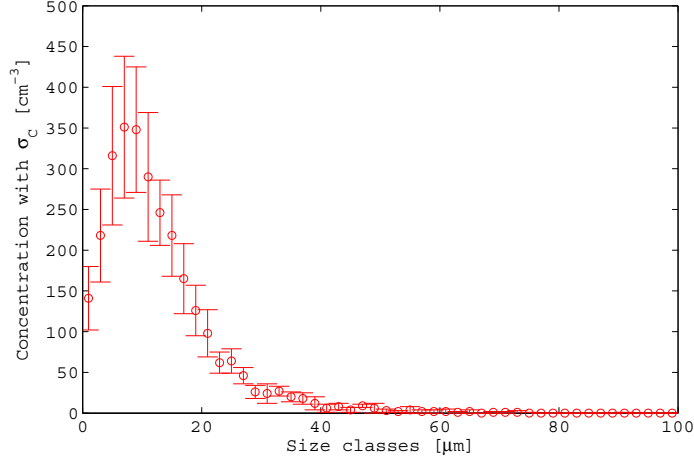


Figure 7: Probability density function of the calculated droplet number density as a function of the size class, including the measured standard deviation as an error bar.

air at the same temperature, $\mathbb{D}(\mathbf{u}) = (\nabla\mathbf{u} + (\nabla\mathbf{u})^T)/2$ is the velocity deformation tensor, and t_e denotes the final time. The gravitational acceleration term is included into the pressure.

The Navier–Stokes equations (2) have to be combined with boundary conditions and an initial condition. The inlet condition at $\Gamma_{\text{in}} = \{0\} \times (-225, 225) \times (-180, 0)$ was directly prescribed using the time-averaged experimental velocity $\mathbf{u}_{\text{exp}}(0, y, z)$ and standard deviation $\sigma_{\text{exp}}(0, y, z)$

$$\mathbf{u}(t, 0, y, z) = \mathbf{u}_{\text{exp}}(0, y, z) + \text{rand}_{\text{normal}}(t, 0, y, z)\sigma_{\text{exp}}(0, y, z)\mathbf{e}_1,$$

where $\text{rand}_{\text{normal}}(t, 0, y, z)$ denotes a normally distributed random number and \mathbf{e}_1 the Cartesian unit vector in x direction. The computation of the random number is performed with the Box–Muller scheme. The second and third component of the inlet velocity are set to be zero. At the outlet $\Gamma_{\text{out}} = \{500\} \times (-225, 225) \times (-180, 0)$, outflow boundary conditions

$$(2\nu\mathbb{D}(\mathbf{u}) - p\mathbb{I}) \cdot \mathbf{n} = \mathbf{0}$$

were used. Here, \mathbf{n} denotes the outward pointing normal vector on the boundary. Along the top boundary $\Gamma_{\text{top}} = \{0, 500\} \times (-225, 225) \times \{0\}$ [m³], a free slip boundary condition without penetration is implemented

$$\begin{aligned} \mathbf{u} \cdot \mathbf{n} &= 0 \quad \text{on } \Gamma_{\text{top}}, \\ \mathbf{n}^T (2\nu\mathbb{D}(\mathbf{u}) - p\mathbb{I}) \boldsymbol{\tau}_k &= 0 \quad \text{on } \Gamma_{\text{top}}, \quad k = 1, 2, \end{aligned}$$

where $(\mathbf{n}, \boldsymbol{\tau}_1, \boldsymbol{\tau}_2)$ is an orthonormal system of vectors. This boundary condition models a symmetry plane. On all other boundaries $\Gamma = \partial\Omega \setminus (\Gamma_{\text{in}} \cup \Gamma_{\text{out}} \cup \Gamma_{\text{top}})$, free slip with penetration conditions were used

$$\begin{aligned} \mathbf{n}^T (2\nu\mathbb{D}(\mathbf{u}) - p\mathbb{I}) \mathbf{n} &= 0 \quad \text{on } \Gamma, \\ \mathbf{n}^T (2\nu\mathbb{D}(\mathbf{u}) - p\mathbb{I}) \boldsymbol{\tau}_k &= 0 \quad \text{on } \Gamma, \quad k = 1, 2. \end{aligned}$$

This boundary conditions model the case that there are fluctuations on Γ which are directed inside and outside the domain. This corresponds to the experimental setup since the measured volume is just inside the wind tunnel and its boundaries

are slightly away from the walls of the wind tunnel. To obtain an initial condition, the flow was simulated until it was fully developed. An instantaneous flow field was then saved and used as initial flow field in all simulations.

The DSD was modeled by a population balance equation. This model includes transport, growth, and agglomeration of droplets. It has the form

$$\begin{aligned} & \frac{\partial f}{\partial t} + \frac{\partial}{\partial d} \left(\frac{a}{d} f \right) + \mathbf{u}_{\text{drop}} \cdot \nabla f \\ &= \frac{d^2}{2} \int_{d_{\min}}^d \frac{\kappa_{\text{agg}} \left((d^3 - (d')^3)^{1/3}, d' \right)}{(d^3 - d'^3)^{2/3}} f \left(\cdot, (d^3 - (d')^3)^{1/3} \right) f(\cdot, d') dd' \\ & \quad - f(\cdot, d) \int_{d_{\min}}^{d_{\max}} \kappa_{\text{agg}}(d, d') f(\cdot, d') dd' \quad \text{in } (0, t_e) \times \Omega \times (d_{\min}, d_{\max}), \quad (3) \end{aligned}$$

where f (m^4) is the droplet size distribution, d (m) is the diameter of the droplets with $d \in [d_{\min}, d_{\max}]$, \mathbf{u}_{drop} (m/s) is the velocity of the droplets, a (m^2/s) is the growth rate, and κ_{agg} (m^3/s) is the aggregation kernel.

Experimental data are available for the time-averaged first component of the droplet velocity at the planes $x = 0$ mm, $x = 200$ mm, and $x = 400$ mm, see Fig. 5. These values are subtracted from the experimental data of the time-averaged velocity of air, giving a time-averaged velocity difference between the dilute (water droplets) and continuous (air) phases. This difference was interpolated in $[0, 400]$ (mm) and the values at the plane $x = 400$ mm were used as extrapolation in the domain $[400, 500]$ mm, extending beyond the measured region. Then, this difference was subtracted from the first component of the velocity computed by the Navier–Stokes equations (2) to define the first (longitudinal) component of the droplet velocity \mathbf{u}_{drop} . The other components of the droplet velocity were just prescribed as the velocity components coming from the solution of Eq.(2).

A model for the growth rate was derived in [35] by considering individual droplets

$$a = \frac{4(S-1)}{\left[\left(\frac{L}{R_\nu T} - 1 \right) \frac{L\rho_L}{KT} + \frac{\rho_L R_\nu T}{D e_s(T)} \right]},$$

where S is the saturation, $L = 2.453 \cdot 10^6$ J/kg the latent heat, $R_\nu = 461.5$ J/(kg K) is the gas constant for water vapor, $T = 293.15$ K is the temperature, $\rho_L = 998.21$ kg/ m^3 is the density of water, $K = 2.55 \cdot 10^{-2}$ J/(m s K) is the thermal conductivity of air at the considered temperature [35], $D = 2.52 \cdot 10^{-5}$ m^2/s is the diffusion coefficient of water vapor in air at $T = 293.15$ K and 100 kPa [35], and $e_s(T) = 2338.54$ Pa is the equilibrium vapor pressure at 293.15 K. The factor 4 occurs in the previous equation because the diameter of the droplets is considered instead of the radius, as in [35]. In all present simulations, a super saturation of 1% ($S = 1.01$), was assumed, which is a typical value for clouds (see Chapter 13 in [33]) and corresponds to an estimation of the maximum value found in the wind tunnel experiments, leading to

$$a = 5.0613 \cdot 10^{-12} \text{ m}^2/\text{s}.$$

The model employed for the aggregation follows [16, 32]. The first term models the production of droplets of diameter d due to the agglomeration of smaller droplets. The second term in the model accounts for the disappearance of droplets of diameter d because of their agglomeration with other droplets. For the aggregation kernel κ_{agg} (in m^3/s), two physical processes (Brownian motion and shear) are combined, leading to the sum of two separate contributions

$$\kappa_{\text{agg}}(d, d') = C_{\text{brown}} \frac{2k_B T}{3\mu} (d + d') \left(\frac{1}{d} + \frac{1}{d'} \right) + C_{\text{shear}} \sqrt{2\nabla \mathbf{u} : \nabla \mathbf{u}} (d + d')^3. \quad (4)$$

Here, $k_B = 1.38065 \cdot 10^{-23}$ J/K is the Boltzmann constant. The two dimensionless model parameters, C_{brown} and C_{shear} , will be later calibrated by fitting the numerical results to experimental data.

The experimental data obtained for the droplet number density n (in no./cm³), see Eq.(1), have to be converted first to a droplet size distribution f (in no./m⁴). This is achieved in the following way. For each class, the number of drops n_i (in no./cm³) is experimentally given as well as its standard deviation $\sigma_{n,i}$ (in no./cm³). Following for instance [35] (Eq.2.3.2), the total number of drops per unit volume of physical space is given by

$$n_{\text{tot}}(t, \mathbf{x}) = \int_{d_{\text{min}}}^{d_{\text{max}}} f(t, \mathbf{x}, d) dd.$$

For the time-averaged values at the inlet, it is

$$n_{\text{tot,in}}(\mathbf{x}) = \int_{d_{\text{min}}}^{d_{\text{max}}} f_{\text{in,exp}}(\mathbf{x}, d) dd = \sum_{i=0}^{n_d} n_i. \quad (5)$$

Assuming $f_{\text{in,exp}}(\mathbf{x}, d)$ to be for each \mathbf{x} a continuous function, the composite mid-point rule of numerical quadrature gives

$$\int_{d_{\text{min}}}^{d_{\text{max}}} f_{\text{in,exp}}(\mathbf{x}, d) dd = \sum_{i=0}^{n_d} \int_{d_i}^{d_{i+1}} f_{\text{in,exp}}(\mathbf{x}, d) dd \approx \sum_{i=0}^{n_d} (d_{i+1} - d_i) f_{\text{in,exp}}(\mathbf{x}, d_{i+1/2}). \quad (6)$$

From Eq.(5) and Eq.(6) follows

$$f_{\text{in,exp}}(\mathbf{x}, d_{i+1/2}) \approx \frac{n_i}{d_{i+1} - d_i} \left[\frac{\text{no.}}{\mu\text{m cm}^3} \right] = 10^{12} \frac{n_i}{d_{i+1} - d_i} \left[\frac{\text{no.}}{\text{m}^4} \right]. \quad (7)$$

For the conversion of the experimental number density to the droplet size distribution, equality in the first step of relation Eq.(7) is assumed and the droplet size distribution is linearly interpolated. The standard deviation is scaled the same way, i.e.,

$$\sigma_{f,i}(\mathbf{x}, d_{i+1/2}) = 10^{12} \frac{\sigma_{n,i}}{d_{i+1} - d_i} \left[\frac{\text{no.}}{\text{m}^4} \right].$$

The initial condition is given by

$$f(0, \mathbf{x}, d) = 0 \quad \text{in } \Omega \times (d_{\text{min}}, d_{\text{max}}),$$

i.e. there are no droplets in the flow domain.

Due to the boundary conditions for the flow field at the boundary Γ , which allow fluctuations on Γ to be directed outside the domain, droplets might leave the computational domain. The transport of droplets through the lateral walls because of fluctuations which are directed into the domain is not taken into account since no experimental data are available for this process. In all numerical studies, it turned out that the loss of droplets due to the outflow through the lateral boundaries is negligible. In addition, because of the positive growth rate, a boundary condition for the smallest droplet size d_{min} is necessary, as a simple model for the nucleation of droplets. For this issue, experimental data are not available. To circumvent this difficulty, an artificial smallest diameter of the droplets is introduced, $d_{\text{min,art}} = 0$ m, and the boundary condition for the inlet are finally set

$$f(t, \mathbf{x}, d) = \begin{cases} f_{\text{in,exp}}(0, \mathbf{x}, d) + \text{rand}_{\text{normal}}(t, \mathbf{x}) \sigma_f(\mathbf{x}, d), & \mathbf{x} = (0, y, z) \in \Gamma_{\text{in}} \\ 0, & \text{at } d = d_{\text{min,art}}. \end{cases}$$

The boundary condition at the inlet is thus defined as a normally distributed perturbation of the time-averaged experimental data which is linearly interpolated. In $[d_{\min, \text{art}}, d_{\min})$, the DSD was set to be $f(d) = 0$. Values of the DSD for such small parameters are needed in the production term of the agglomeration integral since $(d^3 - (d')^3)^{1/3}$ tends to zero for $d' \rightarrow d$. This definition prevents the kernel and the terms in the integrals from being singular.

5 Numerical Methods

The numerical studies presented below are based on non-dimensional equations using the following reference values

$$\begin{aligned} l_\infty &= 1 \text{ m}, \quad u_\infty = 1 \text{ m/s}, \quad t_\infty = \frac{l_\infty}{u_\infty} \text{ s}, \quad p_\infty = \rho u_\infty^2 \text{ Pa}, \quad f_\infty = 10^{12} \text{ 1/m}^4, \\ d_\infty &= d_{\max} = 1.71 \cdot 10^{-4} \text{ m}. \end{aligned}$$

The minimal diameter of the droplets was taken from the experimental data to be $d_{\min} = 10^{-6}$ m.

The domain Ω was triangulated with a $50 \times 45 \times 18$ hexahedral grid, equidistant in each direction. With this grid, the positions of the measurement points were located at nodes. In addition, the mesh for the internal coordinate was chosen in such a way that a direct fitting of the experimental data was possible. Since the data were given for equi-distributed diameters, the grid for the internal coordinate was defined in the same way. Only the interval $(0, d_{\min})$ had a different length.

An implicit time stepping scheme and an inf-sup stable finite element method formed the basis of the discretization of the Navier–Stokes equations (2). As time stepping scheme, the Crank–Nicolson method was applied. This scheme is widely used since it leads to a good compromise between accuracy and efficiency [24]. The length of the equi-distant time step was set to be $\Delta t = 0.001$ s or alternatively $\Delta t = 0.0005$ s with a final time $t_e = 1$ s.

After having applied the Crank–Nicolson scheme and a fixed point iteration as linearization, the equations were discretized in each discrete time with the Q_2/P_1^{disc} finite element method. Hence, the velocity was approximated with continuous piecewise second order polynomials and the pressure with discontinuous piecewise linear functions. This pair of finite element spaces has been identified as one of the best performing finite element approaches for the simulation of incompressible Navier–Stokes equations in numerous studies [11, 17, 19]. On the used grid, this finite element discretization leads to 1 020 201 degrees of freedom for the velocity and to 162 000 degrees of freedom for the pressure. The implementation of the slip and penetration boundary conditions in the framework of finite element methods is described in [18].

Since the flow is turbulent, numerical simulations require the application of a turbulence model. In the simulation presented in Section 6, a finite element variational multiscale (VMS) method was applied [6, 7]. In VMS methods, the scale separation is obtained by projections in appropriate function spaces. In this way, resolved large scales $P\bar{\mathbf{u}}$, resolved small scales $(I - P)\bar{\mathbf{u}}$, and unresolved scales \mathbf{u}' are defined, where $\mathbf{u} = P\bar{\mathbf{u}} + (I - P)\bar{\mathbf{u}} + \mathbf{u}'$, P is an L^2 -projector and I is the identity operator. The resolved scales $\bar{\mathbf{u}}$ will be simulated. The idea of scale separation in resolved and unresolved scales is like in traditional large eddy simulation (LES). However, the application of a projection for defining the scale separation is a fundamental difference to LES, as in LES the large scales are defined by spatial averaging. There are meanwhile a number of realizations of VMS methods, see [9, 25] for overviews. A number of studies show that the VMS approach is com-

petitive with LES methods and that it leads often even to better results, e.g., see [10, 15, 34].

In the simulation presented below, the method from [20] was applied, together with the extension of choosing the projection space adaptively which was introduced in [22]. The VMS methods from [20, 22] require the definition of a tensor-valued projection space and the use of an eddy viscosity model. In the method from [20], the projection space is the same in the whole domain. Usually, piecewise constant tensors (VMS-P0) or discontinuous piecewise linear tensors are applied. Experience shows that the constant tensors should be preferred [21, 25]. An a posteriori and adaptive choice of the projection space was proposed in [22]. This choice is based on an indicator for the local turbulence intensity. In the simulations presented in Section 6, the same parameters in the adaption process were used as suggested in [22].

A main feature of the projection-based VMS methods is that the eddy viscosity model acts directly only on the resolved small scales. This is another fundamental difference to LES methods, where the eddy viscosity model acts on all resolved scales. In a number of studies, it was observed that rather simple eddy viscosity models applied within the framework of VMS methods often lead to good results [10, 14]. In the simulations presented below, the static Smagorinsky model [38] was used

$$C_S \delta^2 \|\mathbb{D}(\bar{\mathbf{u}})\|$$

with $C_S = 0.005$ and δ being the length of the shortest edge of a mesh cell.

The number of grid points for discretizing the equation for the DSD is 3 967 086. In [26, 27], it was shown that different discretizations for this equation might lead to considerably different results for quantities of interest. However, the best method from these studies, a finite element flux-corrected transport scheme from [29], is simply too expensive to be applied on the given grid. Finite element methods require numerical quadrature for assembling the system matrices and the costs of this quadrature grow exponentially with the dimension of the domain. For this reason, an upwind finite difference method, together with a forward Euler time stepping scheme (FWE-FDM) or a backward Euler scheme (BWE-FDM), was used. For the considered experiment, much less differences in the results obtained with different discretizations are expected, since the residence time of the droplets in the domain is much shorter compared with the experiments simulated in [26, 27]. For the Euler schemes, the same time steps were applied as they were used in the temporal discretization of the Navier–Stokes equations.

The evaluation of the agglomeration integrals on the right hand side of Eq.(3) was based on a pre-processing step. This step will now be described exemplarily for the second term in Eq.(3). In this discussion, the dependency of the DSD on time and space will be neglected.

Let $0 = d_0 < d_1 = d_{\min} < \dots < d_N = d_{\max}$ be the grid points with respect to the internal coordinate. As explained above, $f(d)$ vanishes in (d_0, d_1) . Otherwise, the DSD is assumed to be continuous. Then, the integral for the second term in Eq.(3) at the diameter d_j , $j \in \{1, \dots, N\}$, is approximated by

$$\begin{aligned} & f(d_j) \int_{d_{\min}}^{d_{\max}} \kappa_{\text{agg}}(d_j, d) f(d') dd' \\ &= f(d_j) \sum_{i=1}^{N-1} \int_{d_i}^{d_{i+1}} \kappa_{\text{agg}}(d_j, d') f(d') dd' \\ &\approx f(d_j) \sum_{i=1}^{N-1} \frac{f(d_{i+1}) + f(d_i)}{2} \int_{d_i}^{d_{i+1}} \kappa_{\text{agg}}(d_j, d') dd'. \end{aligned}$$

The remaining integrals depend only on the kernel and the grid for the internal coordinate

$$\int_{d_i}^{d_{i+1}} \kappa_{\text{agg}}(d_j, d') dd' = C_{\text{brown}} \frac{2k_B T}{3\mu} \int_{d_i}^{d_{i+1}} (d + d') \left(\frac{1}{d} + \frac{1}{d'} \right) dd' + C_{\text{shear}} \sqrt{2\nabla\mathbf{u} : \nabla\mathbf{u}} \int_{d_i}^{d_{i+1}} (d + d')^3 dd', \quad i = 1, \dots, N - 1.$$

Since the grid is given, the integrals on the right hand side can be computed in a pre-processing step. A similar approach can be performed for the first integral in Eq.(3). For the evaluation of the integrals, the package MAPLE was used, since it was not possible to evaluate all integrals analytically. The numerical computation of the integrals in MAPLE was performed with the option to be exact for 14 digits.

6 Numerical Studies

All simulations were performed with the code MOONMD [23]. Figure 8 presents as an example an instantaneous view of the computed velocity field. It can be clearly seen that the flow in the center of the channel is slower due to the nozzle mount placed upstream of the measurement section. The residence time of a droplet in the measurement volume is typically below 0.5 s.

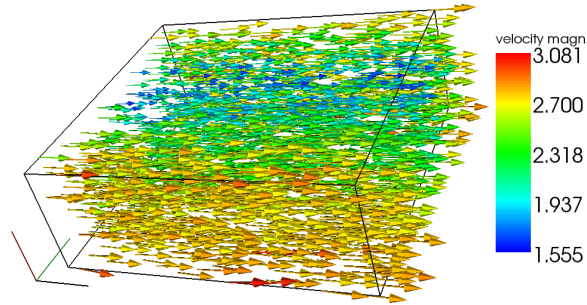


Figure 8: Instantaneous velocity field obtained from the simulation, with the outflow boundary of the measurement section ($x = 400$ mm) on the right hand side.

The main purpose of these numerical studies was the calibration of the unknown parameters C_{brown} and C_{shear} in the aggregation kernel, Eq.(4). In addition, such investigations are useful to quantify the robustness of the results with respect to the different numerical methods presented in the previous section. The calibration was performed by fitting the computed DSD to the experimental data. From the experiments, the DSD was available at each measurement point of the outlet plane ($x = 400$ mm). Due to the turbulent character of the flow, the experimental data, which are already time-averaged, are rather different in different measurement points. For this reason, an averaging in space was applied to the data, leading to one space-time-averaged curve to compare with. The same space-time-averaging was applied for the computational results, where the time averaging was performed in the interval $[0.5, 1]$ s.

Figure 9 presents results for the calibration of the parameters C_{brown} and C_{shear} . After a manual trial and error procedure, it has been found that for appropriately chosen parameters, i.e., $C_{\text{brown}} \simeq 1.5 \cdot 10^6$ and $C_{\text{shear}} \in [0.01, 1]$, the change of the droplet size distribution observed in the experiments from the inlet to the outlet is very well reproduced by the numerical simulations. When considering the order of magnitude difference between C_{brown} and C_{shear} , remember that the term of

the aggregation kernel Eq.(4) referring to Brownian motion contains as well the extremely small factor k_B . For small droplets, the third factor in this term becomes large so that in this case the aggregation associated to Brownian motion dominates, as expected from the physics. On the other hand, for larger droplets (typically for $d \gtrsim 7 \mu\text{m}$), shear-induced aggregation and hence the parameter C_{shear} becomes essential to fit the experimental data correctly (Fig. 9). It should be noted that the used model for the DSD possesses only one direction, namely that larger droplets are created from smaller ones, by aggregation or by growth. Hence, a good prediction of the small droplets is a necessary basis for a good prediction of the large droplets. From the setup of the experiments, it can be expected that aggregation is the dominating mechanism. This dominance was numerically verified by comparing results without the growth term in Eq. (3) and with including this term using a realistic value for the supersaturation. Fig. 10 shows that the impact of the growth term on the simulated DSDs is negligible.

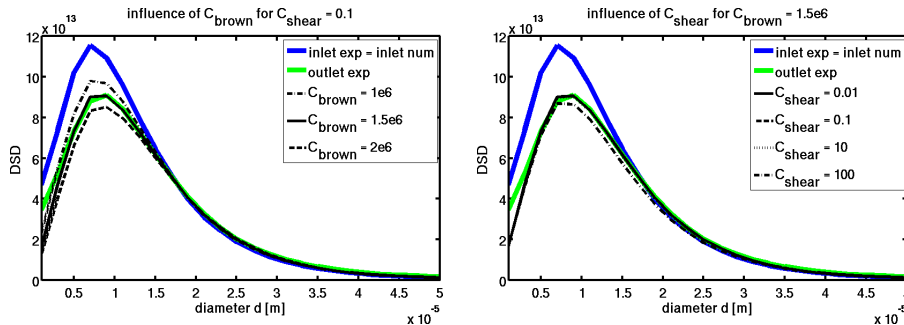


Figure 9: Calibration of the model parameters C_{brown} and C_{shear} , with VMS-ADAP, FWE-FDM and $\Delta t = 0.001$. The green curves are the averaged data at the outlet of the measurement volume.

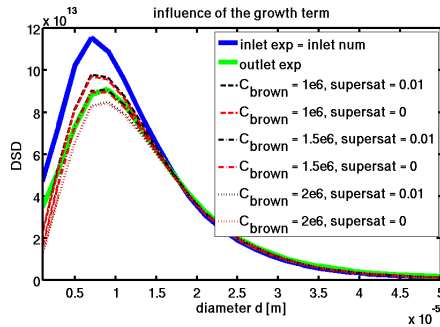


Figure 10: Impact of the growth term in Eq. (3) on the DSD.

The sensitivity of the computed DSD with respect to the various numerical methods is illustrated in Fig. 11. It can be seen that neither the length of the time step, nor the turbulence model, nor the discretization of the equation for the DSD lead to noticeable differences in the results. Hence, the results can be considered to be reliable and the employed numerical techniques are robust.

7 Summary

The properties of a turbulent two-phase flow (air with a spray of water droplets smaller than $50 \mu\text{m}$ in diameter) has been experimentally investigated in a dedi-

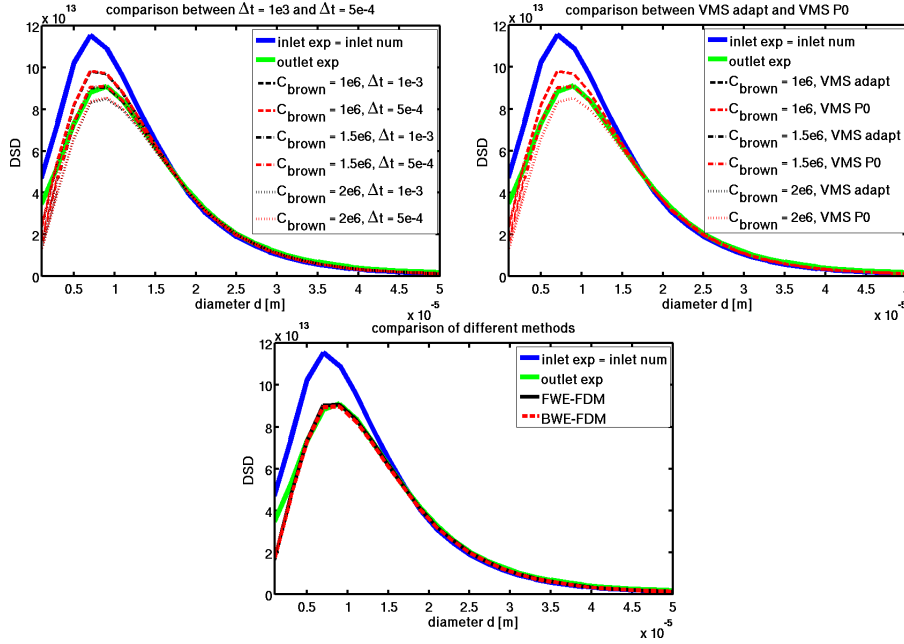


Figure 11: Sensitivity of the DSD. Upper left: with respect to Δt , with VMS-ADAP, FWE-FDM. Upper right: with respect to the turbulence model, with FWE-FDM and $\Delta t = 0.001$. Bottom: with respect to the discretization of the equation for the DSD, with VMS-ADAP and $\Delta t = 0.001$. Note, often the curves are on top of each other.

cated wind tunnel. The velocity of both phases have been measured as well as the Droplet Size Distribution for different positions within the test section. The droplet diameters measured as a function of time have been converted into a droplet number density as a function of different size classes using a post-processing method. The velocity of the air flow, including its temporal change is used as boundary condition for the continuous phase at the inlet, which is modeled by the Navier–Stokes equations. The turbulent flow field is simulated by a finite element variational multiscale (VMS) method.

The measured droplet size distribution (in the form of number density) and velocity information are used in the simulations both as inflow boundary condition for the disperse phase and for a quantitative comparison between experiments and numerical predictions at the outlet. The evolution of the droplet population is modeled by an equation for the DSD, including transport, growth, and aggregation of droplets. The equation for the DSD is defined directly in a 4D domain, including the diameter of the droplets, since the accuracy of the results is more important than the efficiency of the simulations.

After calibrating the unknown parameters of the aggregation kernel by fitting the computed DSD to experimental data, the resulting comparison between experiments and simulations is very promising. Furthermore, the developed numerical techniques appear to be reliable and robust, since neither the length of the time step, nor the turbulence model nor the discretization of the DSD equation lead to noticeable differences in the results, as long as reasonable parameters are considered.

The resulting computational procedure will now be used to investigate in more detail similar issues of increasing complexity, first considering the interaction between two sprays with different initial Droplet Size Distributions, in order to quantify the observed modifications concerning droplet collision and growth. The influ-

ence of the saturation parameter will also be investigated, in parallel to corresponding experiments in the same setup.

References

- [1] R. Bordás, C. Bendicks, R. Kuhn, B. Wunderlich, D. Thévenin, and B. Michaelis. Coloured tracer particles employed for 3D-PTV in gas flows. In J.P. Prenel and Y. Bailly, editors, *13th International Symposium on Flow Visualization*, pages 093/1–093/12, Nice, France, 2008.
- [2] R. Bordás, Gy. Fellegi, B. Wunderlich, R. Kuhn, D. Thévenin, and B. Michaelis. Appropriate tracers to measure velocities in particle-laden gas flows using optical techniques. In (Sommerfeld, M. and Tropea, C.), editor, *6th International Conference on Multiphase Flow, ICMF 2007*, pages S7_Fri_B.66.1–7, Leipzig, Germany, 2007.
- [3] R. Bordás, T. Hagemeyer, and D. Thévenin. Experimental investigation of droplet-droplet interactions. In *23rd European Conference on Liquid Atomization and Spray Systems*, pages 198.1–198.6, Brno, Czech Republic, 2010.
- [4] R. Bordás, T. Hagemeyer, B. Wunderlich, and D. Thévenin. Droplet collisions and interaction with the turbulent flow within a two-phase wind tunnel. *Phys. Fluids*, submitted, 2010.
- [5] R. Bordás and D. Thévenin. Modeling cumulus clouds in a two-phase wind tunnel. In *European Geosciences Union General Assembly EGU 2009*, Vienna, Austria, Poster 4722, 2009.
- [6] M. Farge and K. Schneider. Coherent Vortex Simulation (CVS), a semi-deterministic turbulence model using wavelets. *Flow Turb. Combust.*, 66:393 – 426, 2001.
- [7] M. Farge, K. Schneider, G. Pellegrino, A.A. Wray, and R.S. Rogallo. Coherent vortex extraction in three-dimensional homogeneous turbulence. *Phys. Fluids*, 15:2886 – 2896, 2003.
- [8] S. Ganesan. An operator-splitting heterogeneous finite element method for population balance equations: Stability and convergence. Preprint 1531, WIAS, 2010.
- [9] V. Gravemeier. The variational multiscale method for laminar and turbulent flow. *Arch. Comput. Meth. Engrg.*, 13:249 – 324, 2006.
- [10] V. Gravemeier. Variational multiscale large eddy simulation of turbulent flow in a diffuser. *Comput. Mech.*, 39:477 – 495, 2007.
- [11] P.M. Gresho and R.L. Sani. *Incompressible Flow and the Finite Element Method*. Wiley, Chichester, 2000.
- [12] T. Hagemeyer, R. Bordás, P. Bencs, B. Wunderlich, and D. Thévenin. Determination of droplet size and velocity distributions in a two-phase wind tunnel. In (Bailly, Y. and Prenel J.P.), editor, *ISFV13 - 13th International Symposium on Flow Visualization*, pages 094/1–094/10, Nice, France, 2008.
- [13] Y. Y. Hardalupas and S. Horender. Phase Doppler anemometer for instantaneous measurements of droplet concentration. In *Proceedings of the 10th International Symposium on Application of Laser Techniques to Fluid Mechanics*, pages 23.1.1–13, Lisboa, Portugal, 2000.

- [14] J. Holmen, T.J.R. Hughes, A.A. Oberai, and G.N. Wells. Sensitivity of the scale partition for variational multiscale large-eddy simulation of channel flow. *Phys. Fluids*, 16:824 – 827, 2004.
- [15] T.J.R. Hughes, A.A. Oberai, and L. Mazzei. Large eddy simulation of turbulent channel flows by the variational multiscale method. *Phys. Fluids*, 13:1784 – 1799, 2001.
- [16] H.M. Hulburt and S. Katz. Some problems in particle technology – a statistical mechanical formulation. *Chem. Engrg. Sci.*, 19:555 – 574, 1964.
- [17] V. John. Higher order finite element methods and multigrid solvers in a benchmark problem for the 3D Navier-Stokes equations. *Int. J. Num. Meth. Fluids*, 40:775 – 798, 2002.
- [18] V. John. Slip with friction and penetration with resistance boundary conditions for the Navier–Stokes equations – numerical tests and aspects of the implementation. *J. Comp. Appl. Math.*, 147:287 – 300, 2002.
- [19] V. John. Reference values for drag and lift of a two–dimensional time dependent flow around a cylinder. *Int. J. Numer. Meth. Fluids*, 44:777 – 788, 2004.
- [20] V. John and S. Kaya. A finite element variational multiscale method for the Navier-Stokes equations. *SIAM J. Sci. Comp.*, 26:1485 – 1503, 2005.
- [21] V. John and A. Kindl. Numerical studies of finite element variational multiscale methods for turbulent flow simulations. *Comput. Methods Appl. Mech. Engrg.*, 199:841 – 852, 2010.
- [22] V. John and A. Kindl. A variational multiscale method for turbulent flow simulation with adaptive large scale space. *J. Comput. Phys.*, 229:301 – 312, 2010.
- [23] V. John and G. Matthies. MoonNMD - a program package based on mapped finite element methods. *Comput. Visual. Sci.*, 6:163 – 170, 2004.
- [24] V. John, G. Matthies, and J. Rang. A comparison of time–discretization/linearization approaches for the time–dependent incompressible Navier–Stokes equations. *Comput. Methods Appl. Mech. Engrg.*, 195:5995 – 6010, 2006.
- [25] V. John and M. Roland. Simulations of the turbulent channel flow at $Re_\tau = 180$ with projection–based finite element variational multiscale methods. *Int. J. Numer. Meth. Fluids*, 55:407 – 429, 2007.
- [26] V. John and M. Roland. On the impact of the scheme for solving the higher dimensional equation in coupled population balance systems. *Int. J. Numer. Meth. Engng.*, 82:1450 – 1474, 2010.
- [27] V. John and M. Roland. Simulations of 3d/4d precipitation processes in a turbulent flow field. In G. Kreiss et al., editor, *Numerical Mathematics and Advanced Applications 2009*, pages 479 – 487. Springer, 2010.
- [28] H. J. Kampe. Visibility and liquid water content in clouds in the free atmosphere. *J. Atmosph. Sci.*, 7(1):54–57, 1950.
- [29] D. Kuzmin. Explicit and implicit FEM–FCT algorithms with flux linearization. *J. Comput. Phys.*, 228:2517 – 2534, 2009.

- [30] D.L. Marchisio and R.O. Fox. Solution of population balance equations using the direct quadrature method of moments. *J. Aero. Sci.*, 36:43 – 73, 2005.
- [31] R. McGraw. Description of aerosol dynamics by the quadrature method of moments. *Aerosol Sci. Technol.*, pages 255 – 265, 1997.
- [32] A. Mersmann. *Crystallization Technology Handbook*. Marcel Dekker Inc., New York, 2nd edition, 2001.
- [33] H.R. Pruppacher and J.D. Klett. *Microphysics of Clouds and Precipitation*. Kluwer Academic Publishers, 1997.
- [34] S. Ramakrishnan and S.S. Collis. Turbulence control simulation using the variational multiscale method. *AIAA J.*, 42:745 – 753, 2004.
- [35] R.R. Rogers and M.K. Yau. *Cloud Physics*. Butterworth–Heinemann, 3rd edition, 1989.
- [36] I. V. Roisman and C. Tropea. Drops distribution and flux measurements in sprays using the phase Doppler technique. In *10th International Symposium on Applications of Laser Techniques to Fluid Mechanics*, 2000.
- [37] I. V. Roisman and C. Tropea. Flux measurements in sprays using phase Doppler techniques. *Atomization Sprays*, 11(6):667–700, 2001.
- [38] J.S. Smagorinsky. General circulation experiments with the primitive equations. *Mon. Weather Review*, 91:99 – 164, 1963.
- [39] M. Sommerfeld and H.H. Qiu. Particle concentration measurements by phase-Doppler anemometry in complex dispersed two-phase flows. *Exp. Fluids*, 18(3):187–198, 1995.